

Gaia EDR3 Parallax Zero-point Offset based on W Ursae Majoris-type Eclipsing Binaries

FANGZHOU REN,^{1,2} XIAODIAN CHEN,^{3,4,5} HUAWEI ZHANG,^{1,2} RICHARD DE GRIJS,^{6,7} LICAI DENG,^{3,4,5} AND YANG HUANG⁸

¹*Department of Astronomy, School of Physics, Peking University, Yi He Yuan Lu 5, Hai Dian District, Beijing 100871, People's Republic of China*

²*Kavli Institute for Astronomy and Astrophysics, Peking University, Yi He Yuan Lu 5, Hai Dian District, Beijing 100871, People's Republic of China*

³*CAS Key Laboratory of Optical Astronomy, National Astronomical Observatories, Chinese Academy of Sciences, Beijing 100101, People's Republic of China*

⁴*School of Astronomy and Space Science, University of the Chinese Academy of Sciences, Beijing 101408, China*

⁵*Department of Astronomy, China West Normal University, Nanchong, 637009, China*

⁶*Department of Physics and Astronomy, Macquarie University, Balaclava Road, Sydney, NSW 2109, Australia*

⁷*Research Centre for Astronomy, Astrophysics and Astrophotonics, Macquarie University, Balaclava Road, Sydney, NSW 2109, Australia*

⁸*South-Western Institute for Astronomy Research, Yunnan University, Kunming 650500, People's Republic of China*

ABSTRACT

We independently determine the zero-point offset of the *Gaia* early Data Release-3 (EDR3) parallaxes based on $\sim 110,000$ W Ursae Majoris (EW)-type eclipsing binary systems. EWs cover almost the entire sky and are characterized by a relatively complete coverage in magnitude and color. They are an excellent proxy for Galactic main-sequence stars. We derive a *W1*-band Period-Luminosity relation with a distance accuracy of 7.4%, which we use to anchor the *Gaia* parallax zero-point. The final, global parallax offsets are $-28.6 \pm 0.6 \mu\text{as}$ and $-25.4 \pm 4.0 \mu\text{as}$ (before correction) and $4.2 \pm 0.5 \mu\text{as}$ and $4.6 \pm 3.7 \mu\text{as}$ (after correction) for the five- and six-parameter solutions, respectively. The total systematic uncertainty is $1.8 \mu\text{as}$. The spatial distribution of the parallax offsets shows that the bias in the corrected *Gaia* EDR3 parallaxes is less than $10 \mu\text{as}$ across 40% of the sky. Only 15% of the sky is characterized by a parallax offset greater than $30 \mu\text{as}$. Thus, we have provided independent evidence that the parallax zero-point correction provided by the *Gaia* team significantly reduces the prevailing bias. Combined with literature data, we find that the overall *Gaia* EDR3 parallax offsets for Galactic stars are $[-20, -30] \mu\text{as}$ and $4\text{--}10 \mu\text{as}$, respectively, before and after correction. For specific regions, an additional deviation of about $10 \mu\text{as}$ is found.

Keywords: Parallax (1197) — Eclipsing binary stars (444) — W Ursae Majoris variable stars (1783)
— Catalogs (205) — Milky Way Galaxy (1054) — Close binary stars (254)

1. INTRODUCTION

Gaia's early third data release (EDR3; [Gaia Collaboration et al. 2020](#)) includes astrometric and photometric measurements of more than 1.81 billion sources brighter than $G = 21$ mag. More than 1.46 billion have triangulated parallax measurements with typical uncertainties of 0.03–1.3 mas for stars with $15 < G < 21$ mag. Although the *Gaia* mission represents a leap forward for tests of stellar and Galactic astrophysics, systematic parallax errors are inevitably caused by imperfections in

the instruments and data processing ([Lindegren et al. 2020a](#)). For small parallaxes, the effects of systematic errors are significant, which thus calls for examination of the *Gaia* EDR3 parallaxes using a variety of independent distance tracers.

Comparison of the *Gaia* catalog with other compilations is essential for evaluation of the data quality, and thus to understand *Gaia*'s performance. Special attention has been paid to detecting possible biases. A parallax zero-point offset was noted from the first *Gaia* data release ([Gaia Collaboration et al. 2016](#); [Lindegren et al. 2016](#)); it has since been confirmed (e.g. [Jao et al. 2016](#); [Stassun & Torres 2016](#)). This offset persisted in *Gaia* DR2 ([Gaia Collaboration et al. 2018](#)), ranging from $-29 \mu\text{as}$ to $-80 \mu\text{as}$ (e.g. [Zinn et al. 2019](#)). *Gaia* EDR3 rep-

resents a significant improvement with respect to *Gaia* DR2 (Fabricius et al. 2020) as regards the resulting parallaxes, astrometric parameters, and parallax zero-point corrections.

Lindgren et al. (2020b) published a formal procedure to remove the parallax zero-point offset, which is a function of stellar magnitude, color, and spatial position. Their correction was based on quasars distributed across the entire sky, stars in the Large Magellanic Cloud, and physical binaries. The calibration models differ for astrometric solutions with either five or six parameters. The corrections are most appropriate for sources with similar magnitudes and colors as those in the quasar sample (faint and blue) rather than for typical Galactic stars. Therefore, independent validation of *Gaia* parallaxes based on Galactic objects is urgently needed.

Eclipsing binary systems (EBS) exhibit optical variability because of geometric properties rather than due to intrinsic physical variations. Both components of *W* Ursae Majoris (EW)-type EBS fill their Roche lobes and have similar temperatures. The primary component is similar to a main-sequence star. EWs can be used as distance indicators, because they follow a well-defined period–luminosity relation (PLR; Rucinski & Duerbeck 1997; Chen et al. 2018a). Particularly in infrared (IR) bands, a single EW system can yield a distance with 8% accuracy. In recent decades, the number of known EWs has grown exponentially thanks to new, large surveys (Ren et al. 2021, and references therein).

Here, we use EW distances to investigate the zero-point offset in *Gaia* EDR3 parallaxes. EWs are among the most numerous variables in the Milky Way for which distances can be determined independently. Section 2 introduces our data set, Section 3 presents our method and the main results, and Section 4 discusses our systematic errors and a comparison with literature results. Section 5 summarizes our conclusions.

2. DATA

We used EW data from the American Association of Variable Star Observers International Variable Star Index¹ (Watson et al. 2006). This catalog contains 0.4 million EWs, most of which come from the Zwicky Transient Facility’s (ZTF; Chen et al. 2020) variables catalog. The remainder originate from the All-Sky Automated Survey for Supernovae (ASAS-SN; Jayasinghe et al. 2018), the Asteroid Terrestrial-impact Last Alert System (ATLAS; Heinze et al. 2018), and the Wide-field Infrared Survey Explorer (*WISE*) catalog of periodic variable stars (Chen et al. 2018b).

¹ <https://www.aavso.org/vsx/index.php>

We selected EWs with periods of $-0.55 < \log P$ (days) < -0.25 , which follow a tight PLR, comprising 144,777 objects in *Gaia* EDR3. These EBS were cross-matched with the *WISE* database to obtain *W1* amplitudes. We used the *W1* band to determine their distances, because the extinction in this IR band is much smaller than in optical bands and also since *W1* magnitudes are average EW magnitudes based on ~ 30 independent detections. More importantly, the *W1* PLR is the most accurate EW PLR (Chen et al. 2018a, their Fig. 2). For data quality control, we applied as additional criteria:

1. Renormalized unit weight error (RUWE) ≤ 1.4 ;
2. Blending factor ≤ 1.1 .

The RUWE is equivalent to an astrometric goodness-of-fit indicator. Larger values indicate that the astrometric solution does not completely describe the source motion (Lindgren et al. 2020a; Fabricius et al. 2020); this usually implies the presence of a tertiary companion and, hence, results in significant parallax differences (Stassun & Torres 2021). Although we only consider EWs with RUWE ≤ 1.4 , this will not significantly affect our results (the difference for the overall offset is less than $1\mu\text{as}$). For a typical separation between EW components of $5R_{\odot}$ (Ren et al. 2021), their angular semi-major axis is 0.0048 mas. Since the photocenter’s semi-major axis is clearly smaller than the angular semi-major axis, and because EWs are common-envelope objects with significantly reduced photocenter semi-major axes, the photocenter motion (Stassun & Torres 2021) is negligible in our sample. The blending factor is used to correct *W1* magnitudes and exclude EWs that are significantly affected by bright neighbors in the *W1* band, since the *WISE* angular resolution ($6''$ in *W1*) is worse than that of *Gaia* EDR3 (about $2''$ Lindgren et al. 2020a, their Fig. 6). The blending factor is the ratio of the total *Gaia* *G*-band luminosity of all sources within a $3''$ radius around the target to the target luminosity.

Application of our selection criteria resulted in, respectively, 109,512 and 4309 EWs with five- and six-parameter solutions in *Gaia* EDR3. They are distributed across the full sky, except for small regions near the Galactic Center and in the southern midplane.

3. RESULTS

3.1. PLRs for EWs

Chen et al. (2018a) determined optical-to-mid-IR PLRs based on 183 EWs with *Tycho–Gaia* parallaxes. We rederived the *W1* PLR using *Gaia* EDR3 parallaxes to improve the PLR zero-point. Although only the maximum EW magnitudes, i.e., those outside eclipses, are

directly related to the periods, a tight relationship also exists between mean magnitudes and periods; the dispersion between maximum and mean magnitudes is just $\sigma = 0.05$ mag (Chen et al. 2018a). Our most important reason for deriving the mean-magnitude PLR is that it is more appropriate and convenient for large samples. Maximum magnitudes cannot be determined easily, especially not for EWs collected from different catalogs.

We selected nearby (< 500 pc), bright EWs with accurate parallaxes ($\sigma_\pi/\pi < 0.01$, where π and σ_π are the parallax and its uncertainty, respectively) and $W1$ magnitudes ($\sigma_{W1} < 0.05$ mag). We only consider nearby stars to reduce the systematic error, since the bias (zero-point offset versus parallax) is smaller for nearby stars. The systematic error associated with the zero-point offset in our PLR fits is proportionally reduced when applied to additional EWs (see Section 4.1 for further details). Extinction values were estimated using the three-dimensional (3D) dust reddening map of Green et al. (2019) and $A_{W1}/A_V = 0.039$ (Wang & Chen 2019). We determined absolute magnitudes via $M_{W1} = m_{W1} - 5 \log(1000/\pi) + 5 - A_{W1}$, where the unit of π is mas and m_{W1} is the mean magnitude. The $W1$ PLR was determined from a linear fit to the 1138 objects contained within the 3σ envelope (see Figure 1, top), $M_{W1} = (-6.27 \pm 0.15) \log P$ (days) $- 0.24 \pm 0.07$, $\sigma = 0.16$ mag. The green and blue lines in Figure 1 indicate the linear fit and the 1σ range, respectively.

The average extinction for our 1138 EWs is $A_{W1} = 0.013$ mag ($A_V = 0.322$ mag). This is reliable and appropriate for a sample at an average distance of 368 pc. Considering a 10% uncertainty in the extinction, reflecting uncertainties due to our choice of extinction law, the prevailing systematic bias is around 0.0013 mag.

The G_{BP} and G_{RP} PLRs were determined similarly (see Figure 1, middle and bottom): $M_{BP} = (-10.71 \pm 0.40) \log P - 0.38 \pm 0.19$, $\sigma = 0.43$ mag and $M_{RP} = (-8.98 \pm 0.29) \log P - 0.44 \pm 0.13$, $\sigma = 0.31$ mag. They were used for extinction estimates in the part of the southern sky not covered by the 3D extinction map (see Section 3.2).

3.2. Gaia EDR3 zero-point offset

The $W1$ PLR thus determined can be used to estimate the absolute magnitudes of all EWs. If the extinction is known, we can obtain an object's distance. This distance is affected by the PLR zero-point rather than the *Gaia* parallax zero-point and can therefore be used to determine the systematic offset in the *Gaia* parallaxes. For sources covered by the 3D extinction map, we iteratively obtained the best-fitting extinction, using $A_{W1}(\mu_0) = m_{W1} - M_{W1} - \mu_0$. For

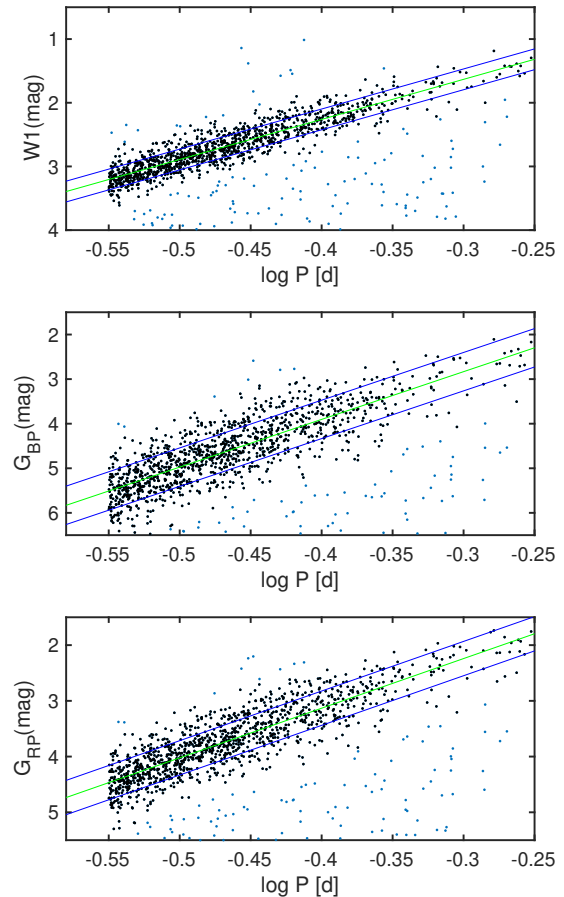


Figure 1. (Top) $W1$, (middle) G_{BP} , and (bottom) G_{RP} PLRs for nearby EWs with accurate parallaxes. Black points: Objects adopted for the PLR determination. Blue dots: Outliers located outside the 3σ envelope. Green line: Best fit. Blue lines: 1σ range.

sources not covered by the 3D extinction map, we estimated the extinction using the G_{BP} and G_{RP} PLRs, i.e. $A_{W1} = \frac{A_{W1}}{A_V} A_V = \frac{A_{W1}}{A_V} \frac{(m_{BP} - M_{BP}) - (m_{RP} - M_{RP})}{\frac{A_{BP}}{A_V} - \frac{A_{RP}}{A_V}}$. Here, μ_0 is the distance modulus, $A_{W1}(\mu_0)$ the extinction at μ_0 , m_λ and M_λ are the apparent and absolute magnitudes in the corresponding band, λ . We adopted the Wang & Chen (2019) extinction law.

Figure 2 shows a comparison of the parallaxes derived from the PLR with those from *Gaia* EDR3. Here, π_{EW} , π_{EDR3} , and π_{EDR3}^{corr} represent parallaxes obtained from PLR distances, *Gaia* EDR3, and *Gaia* EDR3 after zero-point correction based on Lindegren et al. (2020a), respectively. $\Delta\pi_{EDR3} = \pi_{EDR3} - \pi_{EW}$ and $\Delta\pi_{EDR3}^{corr} = \pi_{EDR3}^{corr} - \pi_{EW}$ represent parallax differences.

The parallax differences trace a roughly symmetric, normal distribution with a negative shift, where the *Gaia* parallaxes are systematically smaller. The offsets are $\Delta\pi_{EDR3} = -28.6 \pm 0.6 \mu\text{as}$ and $-25.4 \pm 4.0 \mu\text{as}$, re-

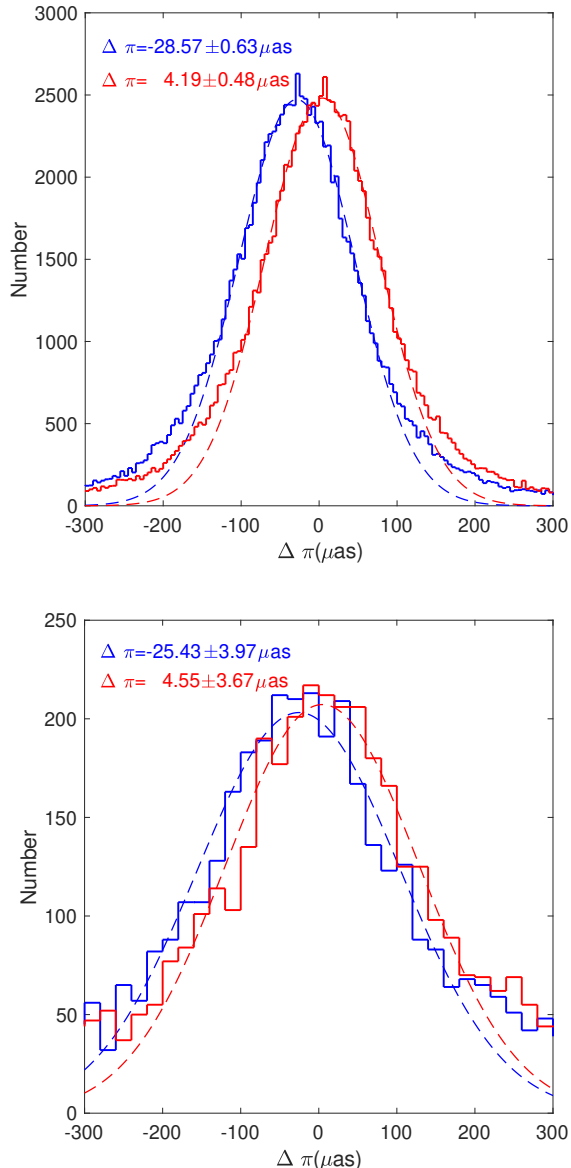


Figure 2. Comparison of predicted parallaxes from the PLR versus *Gaia* EDR3 parallaxes. (top) Objects with five-parameter solutions. The blue and red histograms represent the $(\pi_{\text{EDR3}} - \pi_{\text{EW}})$ and $(\pi_{\text{EDR3}}^{\text{corr}} - \pi_{\text{EW}})$ distributions, respectively. The blue and red dashed lines represent Gaussian fits; the corresponding mean differences are indicated. (bottom) As the top panel, but for six-parameter solutions.

spectively, for the five- and six-parameter solutions (Figure 2, blue histograms), where the errors are the standard deviations. These offsets are slightly larger than that derived from the quasar sample ($-17 \mu\text{as}$ Lindegren et al. 2020b). The $\Delta\pi_{\text{EDR3}}^{\text{corr}}$ distributions are shown as red histograms in Figure 2; the mean values are $4.2 \pm 0.5 \mu\text{as}$ and $4.6 \pm 3.7 \mu\text{as}$ for the five- and six-parameter solutions, respectively. This suggests that the parallax

zero-point correction provided by the *Gaia* team adopting the quasar reference frame significantly reduces the bias in the *Gaia* EDR3 parallaxes, but it may slightly overcorrect the bias for Galactic objects.

Equipped with over 100,000 EWs, we can now assess which parameters contribute to the systematic offset. Figure 3 shows the binned parallax difference distributions, $\Delta\pi_{\text{EDR3}}$ (blue dots) and $\Delta\pi_{\text{EDR3}}^{\text{corr}}$ (red dots), as a function of G magnitude, effective wavenumber, ν_{eff} , ecliptic latitude, $\sin\beta$, and Galactic latitude, $\sin b$, for the five-parameter solutions. Following Lindegren et al. (2020b), we use ν_{eff} as a proxy for the color information. It results from processing of the BP and RP spectra and can be converted directly to $G_{\text{BP}} - G_{\text{RP}}$. The parallax offsets estimated from distant quasars (Lindegren et al. 2020b) are shown as gray points for comparison. Representing one of the largest external comparison catalogs (e.g. Fabricius et al. 2020, their Table 1), the number of EWs is only smaller than the quasar sample. Meanwhile, EWs have good coverage in the Galactic plane, spanning a wide range of colors and magnitudes. The detailed dependence of the parallax differences derived from EWs is fully complementary to that derived from quasar analysis; it is more suitable for Galactic stars.

In Figure 3a, $\Delta\pi_{\text{EDR3}}$ exhibits an increasing, roughly linear trend as a function of magnitude, similar to that shown by the quasars at fainter magnitudes. $\Delta\pi_{\text{EDR3}}^{\text{corr}} \simeq 0$ is stable for $14.5 < G < 17$ mag. Since 55% of our EWs are found in this range, we conclude that the offset analysis based on EWs and quasars is consistent here. In Figure 3b, the $\Delta\pi_{\text{EDR3}}$ trends based on EWs and quasars are consistent for $\nu_{\text{eff}} < 1.5 \mu\text{m}^{-1}$. For effective wavenumbers of $1.5\text{--}1.64 \mu\text{m}^{-1}$, $\Delta\pi_{\text{EDR3}}$ based on EWs is systematically lower by $10\text{--}20 \mu\text{as}$. After correction, $\Delta\pi_{\text{EDR3}}^{\text{corr}} \simeq 0$, but the pattern persists. This effective wavenumber range corresponds to the range of F- and G-type main-sequence stars. The different offsets may be associated with different types of stars and this requires additional data to verify.

We also checked for trends as a function of spatial position. Any trend in $\Delta\pi_{\text{EDR3}}^{\text{corr}}$ with ecliptic latitude is weak (Figure 3c). However, a clear trend is seen as a function of Galactic latitude (Figure 3d). Both $\Delta\pi_{\text{EDR3}}$ and $\Delta\pi_{\text{EDR3}}^{\text{corr}}$ exhibit sharp drops of $10 \mu\text{as}$ in the Galactic plane ($|b| \lesssim 10^\circ$). Elsewhere, $\Delta\pi_{\text{EDR3}}$ and $\Delta\pi_{\text{EDR3}}^{\text{corr}}$ exhibit stable distributions around the mean. This trend is not a result of either extinction or metallicity variations. It is also present for low-extinction sources. Based on 320 EWs with Large-Area Multi-Object Spectroscopic Telescope (LAMOST) metallicity measurements, we obtain $\Delta M_{W1} = M_{W1,\text{obs}} - M_{W1,\text{PLR}} = 0.222[\text{Fe}/\text{H}] + 0.014$ mag. The slope agrees with the near-IR metal-

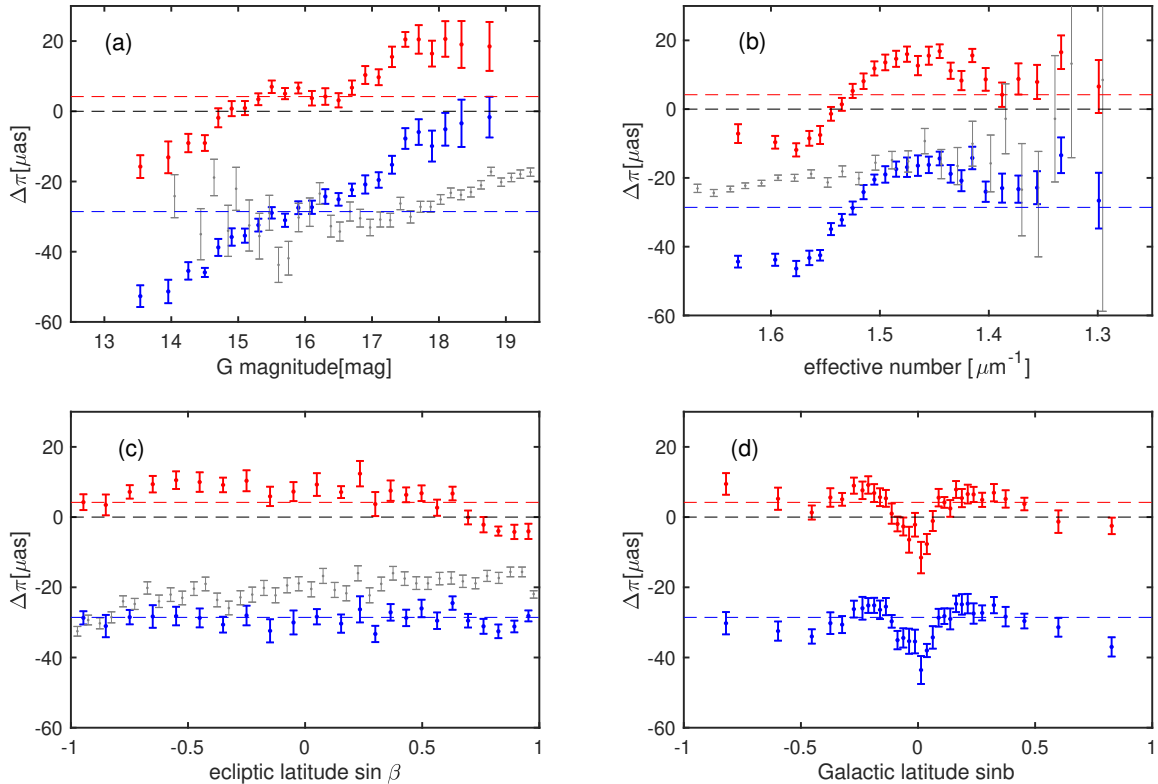


Figure 3. Parallax differences for EWs between the *Gaia* EDR3 five-parameter solution and the PLR as a function of (a) G magnitude, (b) effective wavenumber, ν_{eff} , (c) ecliptic latitude, $\sin \beta$, (d) Galactic latitude, $\sin b$. The blue points and error bars represent the bias in $\Delta\pi_{\text{EDR3}}$; the red symbols pertain to $\Delta\pi_{\text{EDR3}}^{\text{corr}}$, obtained from the best Gaussian fits and their standard deviations. The numbers of stars within each bin exceed 2000. Gray points relate to our quasar control sample (Lindgren et al. 2020b, their Fig. 5). The blue, red, and black dashed lines are the overall offsets in $\Delta\pi_{\text{EDR3}}$ and $\Delta\pi_{\text{EDR3}}^{\text{corr}}$, and the zero deviations, respectively.

licity effect found by Chen et al. (2016). If metallicity effects are taken into account, the trend becomes steeper rather than flatter. Since only quasars with $|b| > 20^\circ$ are used to model the correction for the five-parameter solutions, the correction is reliable for disk sources if the model used for the disk sources is similar to that of the sources at $|b| > 20^\circ$. However, Lindgren et al. (2020a, their Fig. 13) showed that the rise and fall of the parallaxes becomes obvious when they approach the Galactic plane. The likely reason for the trend is, instead, that the correction based on the five-parameter solutions is insufficient for some regions in the Galactic disk.

To better investigate the distribution of the parallax differences as a function of spatial position, maps of $\Delta\pi_{\text{EDR3}}$ and $\Delta\pi_{\text{EDR3}}^{\text{corr}}$ for the five-parameter solutions, in both ecliptic and Galactic coordinates, are shown in Figure 4. The parallax correction varies more significantly with Galactic than ecliptic latitude. The maps are more intuitive to evaluate the corrected *Gaia* EDR3 parallaxes. After correction, the parallax offset is less than $10 \mu\text{as}$ across 40% of the sky, and only 15% of the

sky has a parallax offset greater than $30 \mu\text{as}$. This shows that the correction for *Gaia* EDR3 parallaxes is effective in reducing deviations in the *Gaia* parallaxes.

4. DISCUSSION

4.1. Systematic Errors

Here, we present an estimate of the systematic errors in our PLR-based EW distances. This is important for assessment as to how accurate our derived parallax offset is. The systematic uncertainties include four components, (i) the PLR zero-point offset, (ii) the internal PLR spread, (iii) unresolved third components, and (iv) errors in our extinction estimates.

The $W1$ PLR in Section 2 was obtained based on the parallaxes (calibrated using the five-parameter solution) of 1138 objects located within 500 pc of the Sun. This sample has an average parallax of 3.06 mas . Taking into account the systematic uncertainty of $4.2 \pm 0.5 \mu\text{as}$ (Figure 2), the systematic error propagating to the PLR contributes 0.15%. The systematic error associated with the internal PLR spread is $0.16/\sqrt{1138} = 0.0047 \text{ mag}$, where

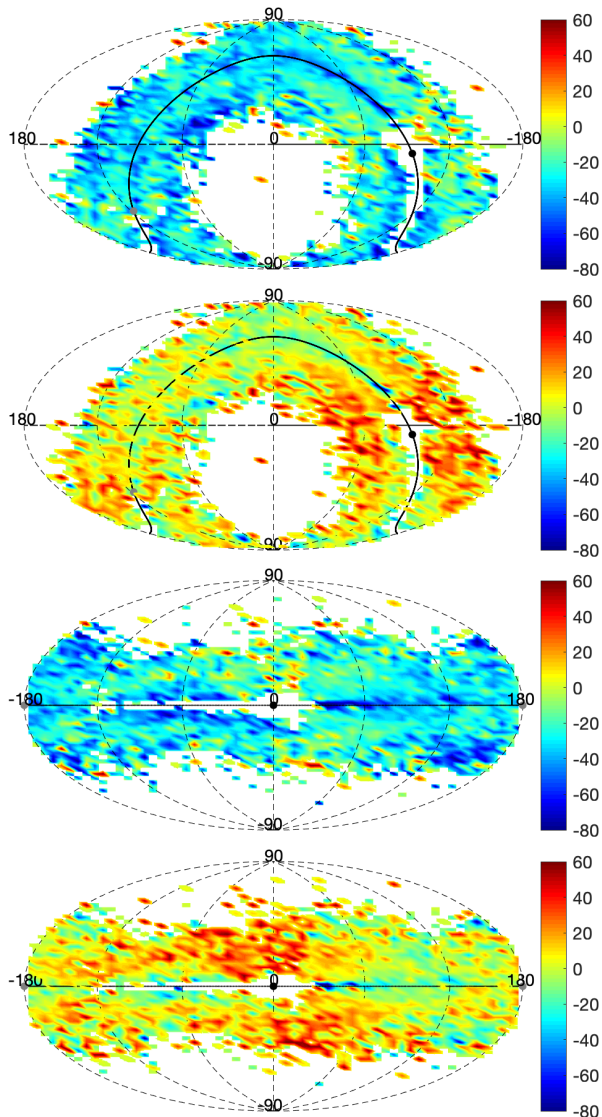


Figure 4. Full-sky maps of the mean parallax differences (units: μas ; color bars) for the five-parameter solutions of $\Delta\pi_{\text{EDR3}}$ and $\Delta\pi_{\text{EDR3}}^{\text{corr}}$. The top two panels show Hammer–Aitoff projections of $\Delta\pi_{\text{EDR3}}$ and $\Delta\pi_{\text{EDR3}}^{\text{corr}}$ in ecliptic coordinates; the bottom two panels are in Galactic coordinates. The resolution of each pixel before smoothing is $3 \times 3 \text{ deg}^2$. We only kept pixels with mean parallax differences estimated from more than 10 EWs. The solid black lines in all panels denote the Galactic plane. The Galactic Center and Anti-Center are shown as black and gray bullets, respectively.

the 1σ dispersion of the $W1$ PLR is 0.16 mag. Based on a study of 75 nearby EWs (D’Angelo et al. 2006), the presence of unresolved third components would affect the parallaxes of our sample objects by 0.3%.

For the adopted extinction, the systematic error is contributed by the extinction difference resulting from application of different methods of extinction determination and the choice of extinction law. Based on 98,466

EWs, the average extinction difference between the 3D extinction map used and the extinction calculated from the G_{BP} and G_{RP} PLRs is $\Delta A_{W1} = 0.0377 - 0.0394 = -0.0017 \text{ mag}$. The average extinction for all EWs is $A_{W1} = 0.035 \text{ mag}$ ($A_V = 0.895 \text{ mag}$), which is reliable for an average distance of 2.41 kpc. Considering a 10% uncertainty in the extinction law, the systematic bias caused by extinction differences is about $\sqrt{0.0035^2 + 0.0017^2} = 0.0039 \text{ mag}$.

We do not consider systematic errors in the PLR caused by metallicity effects, for two reasons. First, our EWs are distributed uniformly around the Sun, at an average distance of 2.4 kpc. EW ages are between 1 Gyr and 10 Gyr, and they do not tend to be distributed preferentially in either the metal-poor halo or the metal-rich Galactic disk. Therefore, the assumption of an average solar abundance for the EW PLR as a whole is appropriate. Second, if metallicity effects are significant, Figure 3d shows that the parallax offset decreases for decreasing $|b|$ (we only consider $|b| > 10^\circ$).

Combining the individual error estimates, the systematic uncertainty affecting our results is $\sigma = 415 \mu\text{as} \times [(0.0015)^2 + (0.0047 \times \ln(10)/5)^2 + (0.003)^2 + (0.0039 \times \ln(10)/5)^2]^{1/2} = 1.8 \mu\text{as}$.

4.2. Comparison

Recently, much work has been done on *Gaia* EDR3 parallaxes based on other tracers. Stassun & Torres (2021) obtained offsets of $-37 \pm 20 \mu\text{as}$ and $-15 \pm 18 \mu\text{as}$, respectively, before and after correction, based on 76 EBS. Huang et al. (2021) found a mean parallax offset of $-26 \mu\text{as}$ based $\sim 70,000$ red clump stars observed with LAMOST, which was reduced to around $4 \mu\text{as}$ after correction. Zinn (2021) and Riess et al. (2021) also found an overestimated zero-point correction of $15 \pm 3 \mu\text{as}$ and $14 \pm 6 \mu\text{as}$ based on, respectively, 2000 first-ascent red-giant-branch stars with asteroseismic parallaxes in the *Kepler* field and 75 classical Cepheids. Ren et al. (2021) found offsets of $-42.1 \pm 1.9 \text{ (stat.)} \pm 12.9 \text{ (syst.)} \mu\text{as}$ and $-10.9 \pm 2.9 \text{ (stat.)} \pm 12.9 \text{ (syst.)} \mu\text{as}$, respectively, before and after correction, based on 2334 EWs in the northern Galactic plane.

Overall, for Galactic stars the *Gaia* EDR3 parallax offsets are $[-20, -30] \mu\text{as}$ and $4\text{--}10 \mu\text{as}$ before and after correction, respectively. For specific regions—the Galactic disk, the bulge, and high-latitude regions—there is an additional deviation of about $10 \mu\text{as}$. Compared with previous results, our new results have smaller errors and higher completeness because of the much larger sample size afforded by our EW sample and their more complete coverage in magnitude, color, and spatial distribution.

5. CONCLUSION

We have used 109,512 and 4309 EWs with five- and six-parameter solutions for an independent examination of the *Gaia* EDR3 parallaxes. Our EWs cover the entire sky, except for the Galactic Center and a small region in the southern Galactic midplane. Representing one of the largest available catalogs, EW types have a relatively complete coverage in magnitude and color.

We determined the *W1* PLR of EWs based on 1194 nearby objects. Adopting this PLR, we obtained independent parallaxes with a 7.4% accuracy to check both the original and zero-point-corrected EDR3 parallaxes. The overall offsets resulting from our analysis are $\Delta\pi_{\text{EDR3}} = -28.6 \pm 0.6 \mu\text{as}$ and $\Delta\pi_{\text{EDR3}}^{\text{corr}} = 4.2 \pm 0.5 \mu\text{as}$ for five-parameter solutions, and $\Delta\pi_{\text{EDR3}} = -25.4 \pm 4.0 \mu\text{as}$ and $\Delta\pi_{\text{EDR3}}^{\text{corr}} = 4.6 \pm 3.7 \mu\text{as}$ for six-parameter solutions, with a systematic uncertainty of $1.8 \mu\text{as}$. The relationships, if any, between the parallax offset and *G*-band magnitude, effective wavenumber, ν_{eff} , ecliptic latitude, $\sin\beta$, and Galactic latitude, $\sin b$, were investigated. The EW results generally agree with those derived from quasars, except for the smaller parallax offsets for effective wavenumbers of $1.5\text{--}1.64 \mu\text{m}^{-1}$ and for stars in the Galactic plane ($|b| \lesssim 10^\circ$). We found that any correlation between parallax offsets and ecliptic latitude is weak.

The spatial distribution of the parallax offsets shows that the bias in corrected *Gaia* EDR3 parallaxes is less than $10 \mu\text{as}$ across 40% of the sky. Only 15% of the sky is affected by parallax offsets greater than $30 \mu\text{as}$. We have thus provided independent evidence that the *Gaia* EDR3 parallax corrections are effective. Combined with literature data, we found that the overall offsets in *Gaia* EDR3 parallaxes for Galactic stars are $[-20, -30] \mu\text{as}$ and $4\text{--}10 \mu\text{as}$, respectively, before and after correction. For specific regions, such as the Galactic disk, the bulge, and high-latitude regions, there is an additional deviation of about $10 \mu\text{as}$. Compared with *Gaia* DR2, the parallax accuracy of *Gaia* EDR3 is thus greatly improved.

We are grateful for research support from the National Key Research and Development Program of China through grants 2019YFA0405500 and 2017YFA0402702. We also received support from the National Natural Science Foundation of China through grants 11903045 and 11973001. This work has made use of data from the European Space Agency's *Gaia* mission (<http://www.cosmos.esa.int/gaia>), processed by the *Gaia* Data Processing and Analysis Consortium (DPAC; <http://www.cosmos.esa.int/web/gaia/dpac/consortium>).

REFERENCES

- Chen, X., de Grijs, R., & Deng, L. 2016, *ApJ*, **832**, 138
- Chen, X., Deng, L., de Grijs, R., et al. 2018a, *ApJ*, **859**, 140
- Chen, X., Wang, S., Deng, L., et al. 2018b, *ApJS*, **237**, 28
- . 2020, *ApJS*, **249**, 18
- D'Angelo, C., van Kerkwijk, M. H., & Rucinski, S. M. 2006, *AJ*, **132**, 650
- Fabricius, C., Luri, X., Arenou, F., et al. 2020, *arXiv*, [arXiv:2012.06242](https://arxiv.org/abs/2012.06242)
- Gaia Collaboration, Brown, A. G. A., Vallenari, A., et al. 2020, *arXiv*, [arXiv:2012.01533](https://arxiv.org/abs/2012.01533)
- Gaia Collaboration, Prusti, T., de Bruijne, J. H. J., et al. 2016, *A&A*, **595**, A1
- Gaia Collaboration, Brown, A. G. A., Vallenari, A., et al. 2018, *A&A*, **616**, A1
- Green, G. M., Schlafly, E., Zucker, C., et al. 2019, *ApJ*, **887**, 93
- Heinze, A. N., Tonry, J. L., Denneau, L., et al. 2018, *AJ*, **156**, 241
- Huang, Y., Yuan, H., Beers, T. C., & Zhang, H. 2021, *arXiv*, [arXiv:2101.09691](https://arxiv.org/abs/2101.09691)
- Jao, W.-C., Henry, T. J., Riedel, A. R., et al. 2016, *ApJL*, **832**, L18
- Jayasinghe, T., Kochanek, C. S., Stanek, K. Z., et al. 2018, *MNRAS*, **477**, 3145
- Lindegren, L., Lammers, U., Bastian, U., et al. 2016, *A&A*, **595**, A4
- Lindegren, L., Klioner, S. A., Hernández, J., et al. 2020a, *arXiv*, [arXiv:2012.03380](https://arxiv.org/abs/2012.03380)
- Lindegren, L., Bastian, U., Biermann, M., et al. 2020b, *arXiv*, [arXiv:2012.01742](https://arxiv.org/abs/2012.01742)
- Ren, F., de Grijs, R., Zhang, H., et al. 2021, *AJ*, **161**, 176
- Riess, A. G., Casertano, S., Yuan, W., et al. 2021, *ApJL*, **908**, L6
- Rucinski, S. M., & Duerbeck, H. W. 1997, *PASP*, **109**, 1340
- Stassun, K. G., & Torres, G. 2016, *ApJL*, **831**, L6
- . 2021, *ApJL*, **907**, L33
- Wang, S., & Chen, X. 2019, *ApJ*, **877**, 116
- Watson, C. L., Henden, A. A., & Price, A. 2006, Society for Astronomical Sciences Annual Symposium, **25**, 47
- Zinn, J. C. 2021, *arXiv*, [arXiv:2101.07252](https://arxiv.org/abs/2101.07252)
- Zinn, J. C., Pinsonneault, M. H., Huber, D., & Stello, D. 2019, *ApJ*, **878**, 136